Molecular outcomes of neuromyelitis optica (NMO)-IgG binding to aquaporin-4 in astrocytes

Shannon R. Hinson[a], Michael F. Romero[b], Bogdan F. Gh. Popescu[c], Claudia F. Lucchinetti[c], James P. Fryer[a], Hartwig Wolburg[d], Petra Fallier-Becker[d], Susan Noell[e], and Vanda A. Lennon[a,c,f,1]

[a]Department of Laboratory Medicine/Pathology, [b]Department of Physiology/Biomedical Engineering, [c]Department of Neurology, and [f]Department of Immunology, Mayo Clinic, College of Medicine, Rochester, MN 55905; and [d]Department of Pathology/Neuropathology and [e]Department of Neurosurgery, University of Tübingen, Tübingen D-72076, Germany

The astrocytic aquaporin-4 (AQP4) water channel is the target of pathogenic antibodies in a spectrum of relapsing autoimmune inflammatory central nervous system disorders of varying severity that is unified by detection of the serum biomarker neuromyelitis optica (NMO)-IgG. Neuromyelitis optica is the most severe of these disorders. The two major AQP4 isoforms, M1 and M23, have identical extracellular residues. This report identifies two novel properties of NMO-IgG as determinants of pathogenicity. First, the binding of NMO-IgG to the ectodomain of astrocytic AQP4 has isoform-specific outcomes. M1 is completely internalized, but M23 resists internalization and is aggregated into larger-order orthogonal arrays of particles that activate complement more effectively than M1 when bound by NMO-IgG. Second, NMO-IgG binding to either isoform impairs water flux directly, independently of antigen down-regulation. We identified, in nondestructive central nervous system lesions of two NMO patients, two previously unappreciated histopathological correlates supporting the clinical relevance of our in vitro findings: (i) reactive astrocytes with persistent foci of surface AQP4 and (ii) vacuolation in adjacent myelin consistent with edema. The multiple molecular outcomes identified as a consequence of NMO-IgG interaction with AQP4 plausibly account for the diverse pathological features of NMO: edema, inflammation, demyelination, and necrosis. Differences in the nature and anatomical distribution of NMO lesions, and in the clinical and imaging manifestations of disease documented in pediatric and adult patients, may be influenced by regional and maturational differences in the ratio of M1 to M23 proteins in astrocytic membranes.

autoimmunity | demyelinating disease | astrocytopathy | intramyelinic edema | antigenic modulation

The most abundant water channel in the central nervous system (CNS) is aquaporin-4 (AQP4), which is confined to astrocytes and ependyma; is enriched at glial–pial and glial–endothelial interfaces; and surrounds nodes of Ranvier and paranodes, adjacent oligodendroglial loops, and synapses (1). In 2005, we identified AQP4 as the target of pathogenic autoantibodies in a spectrum of inflammatory CNS disorders of varying severity that is unified by detection of the serum biomarker neuromyelitis optica (NMO)-IgG (2, 3). These disorders are now recognized collectively as IgG-mediated autoimmune astrocytopathies. Before discovery of this antibody, NMO spectrum disorders were misclassified as multiple sclerosis variants. NMO-IgG is centrally involved in the pathogenesis of NMO spectrum disorders. Its detection predicts frequent relapses that cause cumulative neurological impairment. Lesions characteristically affect the spinal cord and optic nerve, but do not spare the brain. Independent laboratories have demonstrated that NMO-IgG binding initiates AQP4 down-regulation with accompanying endocytosis of its physically associated glutamate transporter, EAAT2, complement activation, impairment of blood–brain barrier integrity, inflammation, and astrocyte injury (4–8). Demyelination is a proposed consequence of both paranodal targeting of AQP4 near oligodendroglial loops (4) and glutamate toxicity to oligodendrocytes (5).

The two major AQP4 isoforms, M1 and M23, have identical extracellular domain residues, but M1 has 22 more amino acids at the cytoplasmic N terminus. Orthogonal arrays of particles (OAPs) containing AQP4 tetramers are an ultrastructural characteristic of membrane specializations on astrocytic foot processes facing sites of rapidly fluxing potassium ions and water (9, 10). OAP size is determined by the M1-to-M23 ratio. In Chinese hamster ovary cells, exogenously expressed M1, without M23, does not form arrays but exists as individual tetramers (10). In the absence of M1, M23 tetramers form high-order arrays in the plasma membrane. When coexpressed, interacting N termini of M1 and M23 form heterotetramers that limit the M23 array size to approximately the size of OAPs in astrocytic membranes (11).

We previously reported that NMO-IgG causes rapid internalization to the endolysosomal compartment of M1 expressed exogenously on the plasma membrane of nonneural (HEK293) cells (4). NMO-IgG also causes AQP4 to redistribute in the plasma membrane of astrocytes and partially internalize, with accompanying reduction in Na^+-dependent glutamate uptake (5). This article reports two novel outcomes of NMO-IgG binding to the AQP4 ectodomain in living cell membranes: differential effects on M1 and M23 proteins and direct blockade of water flux. The multiple potential sequelae of NMO-IgG interactions with AQP4 plausibly account for diverse pathological manifestations of NMO spectrum disorders (including edema, inflammation, demyelination, and necrosis) in different anatomical regions of the CNS (12, 13) and at different stages of CNS maturation in pediatric and adult patients (14).

Results

Astrocytic AQP4 Internalization Is Incomplete Following the Binding of NMO-IgG. In evaluating the dynamics of AQP4 internalization in fetal rat astrocytes exposed to NMO-IgG, we used confocal microscopy to follow AQP4 immunoreactivity (Fig. 1A). Before NMO-IgG exposure, AQP4 was distributed uniformly over the astrocytic plasma membrane, but, within 2 h of adding NMO-IgG, AQP4 redistributed into discrete foci. Aggregates of AQP4 that formed within 2 h did not change appreciably after 16 h of continuous NMO-IgG exposure. Astrocytes derived from neonatal

www.manaraa.com

Fig. 1. Internalization of AQP4 is incomplete in astrocytes exposed to NMO-IgG. (*A*) AQP4 (cyan) and GFAP intermediate filament (magenta) visualized by immunofluorescence before serum exposure (time 0) and after exposure to NMO patient serum. Boxed areas in low-magnification column are enlarged in the adjacent columns. (*B*) AQP4 domains recognized by IgG probes: Rabbit ECD-C-IgG binds to extracellular loop C, and mouse and rabbit AQP4-IgGs bind to intracellular C-terminal residues. N-terminal residues 1–22 are unique to M1. (*C*) AQP4 distribution in fetal rat astrocytes exposed live to NMO patient serum after 20 h. NMO-IgG (cyan) colocalizes with rabbit ECD-C IgG (magenta). Boxed areas designate regions enlarged in right column. (*D*) Localization of AQP4 (magenta) and the early endosomal antigen EEA1 (cyan) before and 10 min after exposure to NMO patient serum. Colocalized probes appear yellow (arrows). Asterisks indicate enlarged boxed areas from merged image. DNA is blue in all merged images. Displayed images represent data from three independent experiments (*A* and *C*) and from two independent experiments (*D*). (Scale bars, 20 μm, pertain to all panels of equal magnification.)

mouse brains yielded similar results. The persistence of astrocytic AQP4 immunoreactivity in the presence of NMO-IgG contrasts with the fate of exogenous M1 expressed on HEK293 cells (4, 5).

To establish whether or not AQP4 foci persisting after extended exposure to NMO-IgG were subplasmalemmal or remained in the plasma membrane, we probed the surface of living astrocytes with rabbit IgG specific for loop C of the AQP4 extracellular domain (ECD-C-IgG, Fig. 1*B*). Fluorochrome-conjugated IgGs mono-specific for rabbit or human IgG revealed that both ECD-C-IgG and NMO-IgG were bound to large clusters of surface AQP4 after 20 h of continuous exposure to NMO-IgG (Fig. 1*C*). To detect internalized AQP4, we probed permeabilized astrocytes before and after exposure to NMO-IgG, with IgGs specific for AQP4 and the early endosome antigen, EEA1, respectively. AQP4 and EEA1 did not colocalize detectably before NMO-IgG exposure (time 0, Fig. 1*D*), but numerous early endosomes contained AQP4 after a 10-min exposure (Fig. 1*D*). These results indicate that, despite AQP4 redistribution and partial internalization into the endosomal compartment following NMO-IgG exposure (Fig. 1*D*), a significant AQP4 fraction resists internalization (Fig. 1*C*).

**IgG-Induced AQP4 Internalization Differs for M1 and M23 Isoforms.** The limited AQP4 internalization that we observed in astrocytes contrasts with our observations in transfected nonneural (HEK293) cells (4). One possible explanation is that there are different internalization dynamics for M1 and M23 isoforms. We therefore investigated rates of M1 and M23 internalization in clonal singly transfected HEK293 cells after exposure to NMO-IgG (Fig. 2*A*). Lysates of each cell type yielded comparable AQP4 protein levels by Western blot analysis (Fig. 2*B*). Confocal microscopy revealed a strong linear pattern of M1 and M23 immunoreactivities in the plasma membrane before NMO-IgG exposure and minimal cytoplasmic staining (Fig. 2*A*). Linear membrane staining was lost from M1 cells within 2.5 h of adding NMO-IgG, and at 4.5 h (Fig. 2*A*) residual immunoreactivity was confined to cytoplasmic vesicles. By contrast, M23 was redis-

tributed in the plasma membrane at 4.5 h, but large patches remained. At 6.5 h, M23 surface clusters were still abundant, but M1 was undetectable except in small cytoplasmic vesicles (Fig. 2*A*, arrow). After 16 h, M23 remained in punctate surface foci reminiscent of those observed in astrocytes (Fig. 1*A*); residual M1 was minimal. These results imply that, following surface cross-linking by NMO-IgG, M1 is removed from the plasma membrane more efficiently than M23. It has been postulated that M23 turnover is slower than M1 due to its incorporation into OAPs (15). Our findings suggest that OAP abundance and composition may determine the consequences of NMO-IgG binding to M1 or M23 tetramers in the astrocytic plasma membrane.

M23 in Cultured Astrocytes Resists NMO-IgG–Induced Internalization. Because M1 internalization is more rapid and complete than M23 internalization, we hypothesized that the limited AQP4 internalization observed in astrocytes is due to predominance of the M23 isoform. We evaluated the relative abundance of each AQP4 isoform in rat astrocytic plasma membranes by Western blot before and after NMO-IgG exposure. We prepared control membranes from nontransfected HEK293 cells and cells transfected singly with M1 or M23. M23 was the predominant AQP4 isoform in astrocytes exposed to control human serum (Fig. 2*C*). After NMO-IgG exposure, both isoforms were reduced relative to actin, but M1 was barely detectable, even after extended autoradiographic exposure (asterisk). Densitometry (Fig. 2*D*) revealed that remaining M1 was ~14% of control values and remaining M23 was 43% ($P = 0.0005$). We conclude that NMO-IgG binding causes internalization (and degradation) of singlet M1 tetramers, that internalization of M23 is limited to small, more mobile OAPs containing M1, and that remaining M23 is in OAPs that are coalesced by NMO-IgG into large-surface aggregates.

NMO-IgG Binding Promotes Intramembranous OAP Aggregation in Living Astrocytes. Our results suggest that the binding of NMO-IgG to surface M23 induces formation of intramembranous
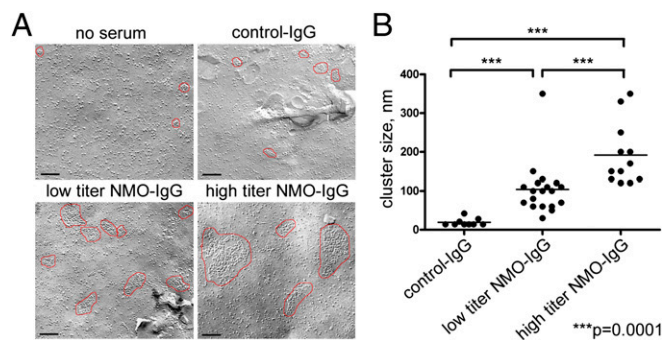
Hinson et al.

www.manaraa.com
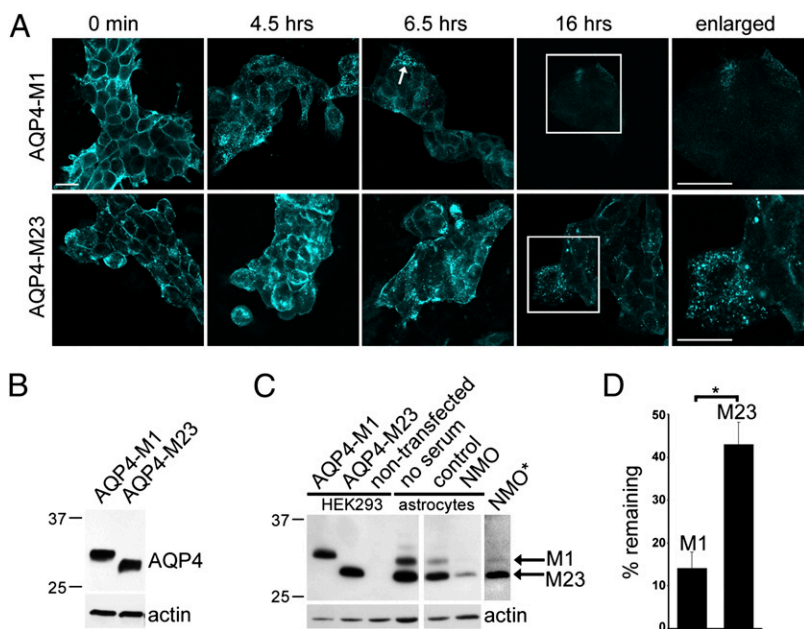
Fig. 2. NMO-IgG binding internalizes M1 more efficiently than M23. (*A*) Distribution of AQP4 in HEK293 cells exogenously expressing M1 or M23 before and after exposure (37 °C) to NMO patient serum and representative of three experiments. Boxed region is enlarged at right. (Scale bars, 20 μm.) (*B*) Western blot shows AQP4 in lysates of HEK293 cells expressing M1 or M23. Actin serves as protein loading control. (*C*) Western blot shows AQP4 in lysates of astrocytes and control HEK293 cells. Astrocytes predominantly express M23. Exposure to NMO serum reduces M1 more than M23 (asterisk: extended autoradiographic exposure). (*D*) Quantification of three Western blot experiments. Bars indicate relative amounts of M1 and M23 remaining after exposure to NMO serum relative to control serum (*$P = 0.003$).

structures that resist internalization. To investigate whether NMO-IgG binding changes the abundance or size of OAPs, we analyzed neonatal mouse astrocytic membranes by freeze-fracture electron microscopy before and after in vitro exposure to human IgG. In the absence of human IgG, intramembranous particles in the nonpolarized membranes of cultured astrocytes were numerous, but OAPs, an ultrastructural characteristic of astrocytic foot processes in vivo (10), were sparse (Fig. 3*A*, encircled in red). Exposure to control patient IgG for 24 h did not alter the membrane architecture appreciably; OAPs were smaller than 50 nm. In contrast, after exposure to IgG prepared from NMO serum of relatively low AQP4-binding capacity (20 nmol/L), OAP clusters of modest size were readily apparent (mean = 104 nm; range, 30–350; $n = 19$). OAP clusters in membranes exposed to IgG prepared from NMO serum with
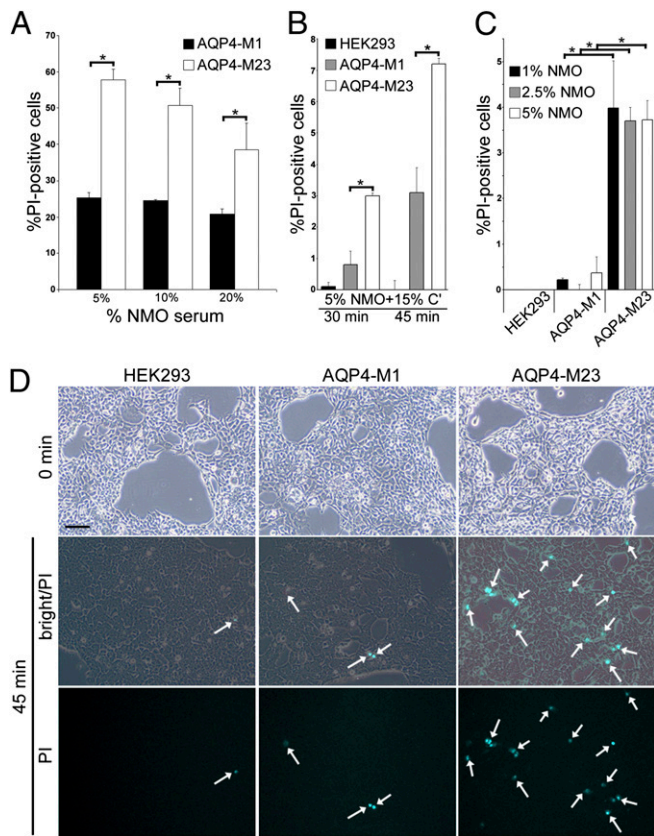
fivefold greater AQP4-binding capacity (105 nmol/L) were of larger size (mean = 190 nm; range, 120–350; $n = 12$, $P = 0.0001$) (Fig. 3*B*). The dose-dependent increase in size of OAPs is consistent with IgG cross-linking. We conclude that NMO-IgG induces rapid and near complete internalization of tetrameric M1 particles and clustering of OAPs, which are composed predominantly of M23, into large assemblies that resist internalization. Large assembly formation, which is facilitated by M1 deficiency (10), would provide an optimal membrane target for activation of complement by bound IgG.

When Complement is Limited, NMO-IgG Bound to M23 Activates More Effectively than NMO-IgG Bound to M1. We investigated complement activation by M1 and M23 via flow cytometric analysis of propidium iodide (PI) permeability after incubating singly transfected HEK293 cells with graded concentrations of NMO serum (4). When serum and complement exposures were sequential, M23 cells consistently activated complement more than M1 cells (Fig. 4*A*). To minimize loss of M1 epitope density by IgG-induced internalization, we next exposed the cells to serum and complement simultaneously. Again, M23 cells activated complement more effectively than M1 cells (Fig. 4 *B* and *C*). To prevent fragmentation of M23 cells and enable more accurate counting of lesioned cells, we limited NMO serum concentration to 5% and complement to 15%. NMO-IgG consistently yielded twofold more PI-positive M23 cells than M1 cells did (Fig. 4*B*). To compare the relative sensitivities of M23 and M1 cells to lesioning by complement, we reduced the concentrations of NMO serum and complement to 1% and 10%. The number of PI-positive cells increased in the M23 population, but not in the nontransfected or M1 population (Fig. 4*C*). The efficacy of complement activation by M23 cells was readily visualized by phase-contrast microscopy (Fig. 4*D*). PI positivity was rare in nontransfected cells and was detected occasionally in M1 cells and frequently in M23 cells.

NMO-IgG Binding Blocks the AQP4 Water Channel. To investigate the effect of NMO-IgG on AQP4 water fluxes, we tested the outcome of NMO-IgG binding to AQP4 in the *Xenopus laevis* oocyte system (16). By Western analysis, oocytes injected with cRNAs encoding M1 or M23 expressed equivalent protein levels (Fig. 5*A*). Immunofluorescence revealed plasma membrane localization of M1, M23, and control AQP1, where each was tightly confined at ambient temperature (22 °C) (Fig. 5*B*). Oocytes injected with vehicle or AQP1 cRNA lacked AQP4 immunoreactivity. After exposure to NMO-IgG at 22 °C, M1 and M23 appeared more punctate and M1 was prominent in subplas-

Fig. 3. (*A*) Freeze-fracture electron microscopic analysis of mouse astrocytes cultured without and with IgG from control or NMO serum. Unexposed or exposed to control human IgG (∼2 mg/mL), most intramembranous particles are single and distributed uniformly. OAPs (encircled in red) are small and relatively sparse. After exposure for 24 h to IgG prepared from "low-titer" NMO serum (AQP4-binding capacity = 20 nmol/L), OAPs are modestly larger. After exposure to "high-titer" serum IgG (AQP4-binding capacity = 105 nmol/L), OAPs are much larger. (Scale bars, 100 nm.) (*B*) Scatter plot analysis of OAP size after exposure to control-IgG or NMO-IgG of low or high titer. Horizontal bars correspond to mean values. Differences between values for control-IgG and low-titer NMO-IgG and control-IgG and high-titer NMO-IgG and between low-titer and high-titer NMO-IgG are significant (***$P = 0.0001$). Differences for OAP cluster sizes in control-IgG and low-titer and high-titer NMO-IgG were compared by the Mann–Whitney test with GraphPad software.

Hinson et al.

Fig. 4. M23 interaction with NMO-IgG activates complement more effectively than M1. Simultaneous addition of complement and heat-inactivated NMO serum caused rapid lysis of HEK293 cells expressing M1 or M23. Therefore, for flow cytometric analysis cells were exposed sequentially to serum (30 min at 22 °C) and complement (45 min at 37 °C) (4). Lesioning (PI permeability) was negligible with heat-inactivated complement (values subtracted). Bars represent SEMs of three or more experiments. (*A*) Cells exposed to graded concentrations of NMO serum and 20% complement. Membrane lesioning was maximal with 5% NMO serum [M1 compared with M23; *$P < 0.001$ (5%); *$P < 0.001$ (10%); *$P = 0.013$ (20%)]. (*B*) To circumvent M1 internalization by NMO-IgG at 37 °C, we simultaneously added 5% serum and complement at suboptimal concentration (15%). M23 cells showed consistently greater vulnerability to lesioning [*$P = 0.031$ (30 min); *$P = 0.013$ (45 min)]. (*C*) With complement limited to 10% concentration for 45 min, its activation by M23 cells was consistently fourfold more than by M1 cells at all tested NMO serum concentrations [*$P = 0.05$ (1%); *$P = 0.001$ (2.5%); *$P = 0.005$ (5%)]. (*D*) Phase-contrast microscopy appearance of PI permeable cells (cyan; arrows) under conditions shown in *B* (nontransfected and transfected with M1 or M23). (Scale bar, 200 μm.)

malemmal vesicles (arrows, Fig. 5*B*), consistent with greater internalization of M1 than M23. By contrast, all three AQP proteins remained tightly localized to the plasma membrane at 4 °C, regardless of IgG exposure (Fig. 5*B*).

Oocyte lysis time was an indicator of water influx. All oocytes expressing exogenous AQP lysed within 60 s of exposure to water (Fig. 5*C*), but vehicle-injected oocytes resisted hypotonic stress for more than 1,500 s. After 4 h exposure at 22 °C to either control-IgG or NMO-IgG, lysis time was unchanged for oocytes lacking exogenous AQP or expressing AQP1 (Fig. 5*C*). However, lysis times for oocytes expressing M1 or M23, or both, were significantly extended after NMO-IgG exposure, but not after control-IgG exposure (Fig. 5 *C* and *D*). Oocytes expressing M1 or both M1 and M23 were twofold more resistant than oocytes exposed to control-IgG; oocytes expressing M23 alone were 1.5-fold more resistant (Fig. 5*D*). These results support the immunostaining data (Fig. 5*B*) and data from mammalian cells (Figs. 1 and 2) that antigen down-regulation is greater for M1 than for M23. The similar outcomes for oocytes expressing M1, alone or

with M23, are consistent with the ability of M1 to disrupt OAP formation by M23.

Because endocytosis is inhibited at 4 °C in *Xenopus* oocytes (17), we evaluated the direct effects of NMO-IgG binding on water influx at <4 °C (on a wet ice bath), a temperature that would prevent IgG-induced AQP4 internalization (Fig. 5*E*). Again, NMO-IgG exposure did not affect lysis times for oocytes lacking an AQP or expressing AQP1 compared with control-IgG. However, NMO-IgG conferred a 1.5-fold increase in resistance to hypotonic stress compared with control-IgG on oocytes expressing AQP4 of either isoform, singly or combined (Fig. 5*E*). These results suggest that NMO-IgG binding to the AQP4 ectodomain directly reduces water influx.

Immunohistopathological Observations in Nondestructive NMO Lesions Compatible with Focal Resistance of Astrocytic AQP4 Internalization and Disrupted Water Homeostasis. Our in vitro findings support new interpretation of lesional observations not previously emphasized in CNS tissues of NMO patients. Fig. 6 shows histopathological specimens obtained from two NMO-IgG–seropositive patients. In the first illustrative patient, a nondestructive forebrain lesion exhibits characteristic loss of AQP4 immunoreactivity (Fig. 6*A*). Foci of persisting AQP4 are seen in association with the plasma membrane of phenotypically reactive astrocytes within that lesion (Fig. 6 *B–D*; swollen cell bodies, clear cytoplasm, and prominent nuclei are indicated by black arrows). Cerebellar tissue from the second patient shows edema within myelin near a nondestructive lesion (Fig. 6*E*). Intramyelinic edema is the predicted outcome of water homeostasis disruption through binding of NMO-IgG to astrocytic AQP4 in the adjacent lesion. Higher magnification of that lesion shows patches of residual AQP4 immunoreactivity on the astrocytes, consistent with incomplete internalization (Fig. 6*F*, arrow).

Discussion

Our study has revealed that both AQP4 internalization and complement activation are largely isoform-dependent outcomes of NMO-IgG binding (Figs. 1–4). Binding to extracellular epitopes of densely packed OAPs (i.e., M23) activates complement more effectively than binding to dispersed M1 tetramers. In contrast, binding to tetrameric M1 induces rapid AQP4 internalization. We postulated that M23 residing in smaller arrays containing M1 was internalized while M23 residing in larger OAPs consisting mostly of M23 was resistant to internalization. It is plausible that removal of M1 from the plasma membrane through NMO-IgG–induced internalization triggers coalescence of the remaining M23 into the larger arrays that we observed by freeze-fracture. Either scenario would result in large M23 arrays that are an ideal substrate for complement activation.

The quiescent CNS compartment in which NMO-IgG initially encounters AQP4 lacks the C1q component of complement essential for Ig-dependent (classical) pathway activation (18). In that environment, rapid down-regulation of surface M1 would protect the astrocyte from subsequent lysis by its own up-regulated production of complement components (16) (a consequence that we predict would be initiated by surface cross-linking of AQP4). Residual arrays of NMO-IgG bound to internalization-resistant M23 would potently activate subsequently secreted complement components. In a clinical context, we have documented a positive correlation between NMO severity and AQP4-dependent complement activation by patient sera (19). We conclude that the extent of complement activation is determined synergistically by the M1-to-M23 ratio in the astrocytic membrane, the regional abundance of complement, and the epitope specificities of the individual patient's NMO-IgG.

The multiple molecular outcomes of NMO-IgG interactions with AQP4 provide pathophysiological insights for the evolution of CNS lesions in NMO spectrum disorders. We have demonstrated that NMO-IgG binds to both M1 and M23 isoforms. Biophysical measures have demonstrated that M23 tetramers in OAPs have more restricted plasma membrane mobility than M1 tetramers (20). The observations that we report here predict that AQP4 internalization would be limited in CNS regions with relatively high M23 expression. Where M1 is abundant, OAP size

Hinson et al.

Fig. 5. NMO-IgG binding inhibits water influx through AQP4. (*A*) Western blot analysis shows relative levels of AQP4 protein in cRNA-injected oocytes. Each lane represents lysates from approximately four oocytes. (*B*) Immunofluorescence staining of M1, M23, and AQP1 in plasma membranes of cRNA-injected oocytes exposed to control-IgG or NMO-IgG. At 4 °C, regardless of human IgG, and at 22 °C with control human IgG, all AQP immunoreactivities are tightly confined to the plasma membrane. At 22 °C with NMO-IgG, AQP1 is unchanged, but AQP4 M1 and M23 immunoreactivities are more punctate (asterisks), and M1 is visibly associated with subplasmalemmal vesicles (arrows). (Scale bar, 10 μm, pertains to all panels.) (*C*) Representative hypotonic stress assay (immersion in distilled water) shows oocyte lysis times (seconds) after exposure to control-IgG or NMO-IgG for 4 h at 22 °C. Each condition included 5–12 injected oocytes. Injected cRNAs are indicated below the graph. Asterisks indicate significance in comparing oocytes exposed to control-IgG and NMO-IgG for M1 ($P < 0.001$), M23 ($P = 0.005$), and M1 + M23 ($P < 0.001$). (*D* and *E*) Cumulative data from five to six hypotonic stress assays show fold increase in lysis times for oocytes exposed to NMO-IgG relative to lysis times for oocytes exposed to control-IgG at 22 °C or 4 °C. (*D*) Asterisks indicate P values relative to AQP1 controls: M1 ($P < 0.001$), M23 ($P < 0.001$), M1 + M23 ($P < 0.001$), and relative to M23—M1 ($P = 0.032$) and M1 + M23 ($P = 0.016$). (*E*) Comparisons are relative to AQP1: M1 ($P = 0.028$) and M23 ($P = 0.001$); differences between M1 and M23 were not significant.
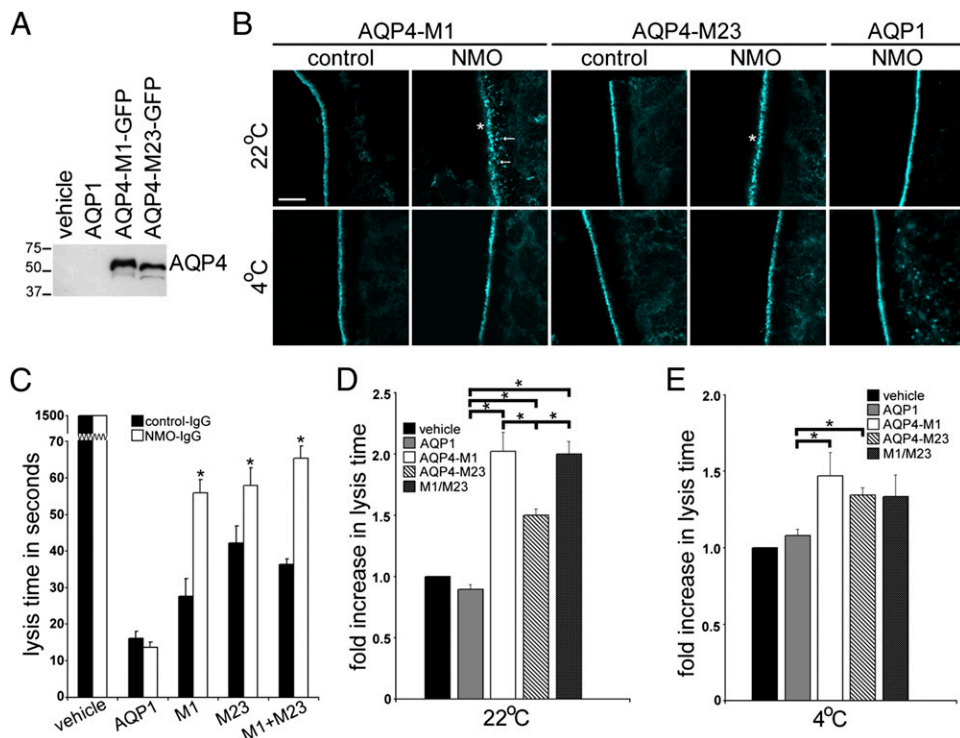
would be smaller and AQP4 mobility in the plasma membrane greater, thus favoring AQP4 internalization rather than complement activation. When complement is unavailable or inactivated by complement-regulatory proteins, the major anticipated pathophysiological outcome would be disruption of water homeostasis either by direct blockade of water flux and by AQP4 internalization. NMO-characteristic periventricular abnormalities that rapidly reverse with high-dose corticosteroid therapy have been documented by magnetic resonance imaging and are attributed to tissue water accumulation (21, 22). The striking parenchymal edema that we observed in NMO histopathological lesions is consistent with these interpretations.

Formation of exceptionally large aggregates of OAPs by IgG cross-linking of smaller arrays of M23 particles may limit M23 internalization. Clathrin-mediated endocytosis is typically restricted to particles smaller than 120 nm, while internalization by caveola-dependent pathways, and by pathways independent of clathrin or caveolin, is restricted to even smaller particles (23). The large size of OAPs induced in cultured astrocytes by NMO-IgG (on average 190 nm; Fig. 3) plausibly accounts for their limited internalization.

The data that we present increase the complexity of antigen-specific NMO therapeutic strategies. For example, high-affinity monoclonal IgG fragments reactive with autoantigen ectodomains have been shown, in experimental myasthenia gravis, to protect target plasma membranes from pathogenic sequelae of autoantibody interactions (24). In theory, a noncomplement-activating AQP4-specific monoclonal IgG could prevent inflammatory and necrotic sequelae of NMO-IgG binding to CNS targets. However, divalent fragments would not prevent internalization of M1 (and coupled EAAT2), and monovalent fragments may impair water homeostasis in critical CNS locations.

Materials and Methods

Astrocytes, Cell Lines, and Transgenic Constructs. Astrocyte cultures were established from cerebral cortices of fetal (embryonic days 18–21) rats or newborn mice (25). M1 and M23 cDNAs and stably transfected clones of HEK-293 were produced as described (2, 4). DNA encoding AQP4 extra-

cellular loop C was PCR amplified and cloned into pET 4T vector (Stratagene) to produce and purify GST-ECD-C fusion protein (26).

Antibodies and Sera. Fluorochrome-conjugated secondary antibodies were from Southern Biotechnology. Rabbit anti-AQP4 C terminus IgG and Cy3-MAb IgG anti-GFAP were from Sigma, anti-EEA1 MAb IgG was from BD Biosciences, and rabbit anti-actin and anti-AQP1 C terminus IgGs were from Santa Cruz and Abcam. Rabbit anti-AQP4 loop C and mouse anti-AQP4 C terminus MAb IgGs were made in-house. Pools of ~50 de-identified NMO and control patient sera were obtained from the Neuroimmunology Laboratory, Department of Laboratory Medicine/Pathology, at the Mayo Clinic.

Immunostaining. Cells were grown and immunostained as described (4, 5). Confocal images were captured using a Zeiss LSM510 confocal microscope with a 63× water immersion lens. Detailed procedures are provided in *SI Materials and Methods*.

Antigen Modulation Assay. Serum or IgG was added to cells grown on coated glass coverslips for at least 48 h. Complement was inactivated by holding 30 min at 56 °C. See *SI Materials and Methods*.

Complement Activation Assay. NMO or control sera were added in growth medium. After 30 min at 22 °C, fresh or heat-inactivated complement was added (Low–Tox-H, Cedarlane Laboratories). After 45 min at 37 °C, cells were analyzed by flow cytometry (4).

Freeze-Fracture Electron Microscopy. Primary mouse astrocyte monolayers were fixed (2 h, 22 °C) with 2.5% glutaraldehyde in 0.1 M cacodylate buffer (pH 7.4), cryoprotected in 30% glycerol, and quick-frozen in nitrogen slush (−210 °C). Specimens were fractured in a freeze-fracture device (BAF400D; Balzers) at 5×10^{-6} mbar and −150 °C. Fracture faces were shadowed with platinum/carbon (2.5 nm, 45 °C) for contrast and with carbon (25 nm, 90 °C) for replica stabilization. After removing cell material in 12% sodium hypochlorite, replicas were cleaned in double-distilled water and mounted on Pioloform-coated copper grids. Replicas were examined under a Zeiss EM10 electron microscope.

Oocyte Isolation and Injection. Oocytes were removed from *X. laevis* frogs (*Xenopus* Express), dissociated with collagenase (27), and studied 3–6 d after
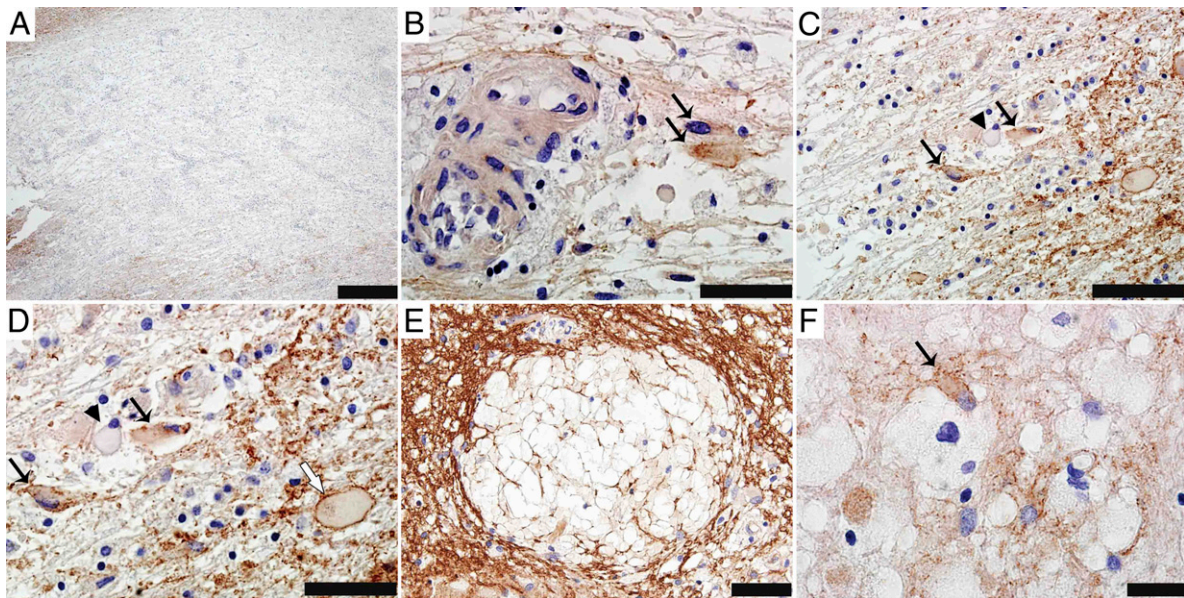
Fig. 6. Immunohistopathological observations in NMO lesions reveal nonlytic astrocytic changes compatible with newly documented in vitro outcomes of NMO-IgG interacting with AQP4. Brain tissues from two seropositive NMO patients reveal incomplete internalization of surface AQP4 in astrocytes and tissue vacuolation. Forebrain autopsy (*A–D*) and cerebellar biopsy (*E* and *F*) with immunoperoxidase/hematoxylin stain. (*A*) NMO lesion (patient 1) shows characteristic loss of AQP4 immunoreactivity (brown) (Scale bar, 500 μm.) (*B*) Reactive astrocytes with incomplete AQP4 internalization (arrows) adjacent to blood vessels in the same NMO lesion (Scale bar, 33 μm.) (*C*) Some astrocytes in this lesion (arrows) also have AQP4 in cytoplasmic vesicles. Reactive astrocytes with complete AQP4 loss (arrowhead) are also visible (Scale bar, 50 μm.) (*D*) Higher magnification of *C* shows lesional astrocytes with partial AQP4 internalization (black arrows), or complete AQP4 loss (arrowhead), and an astrocyte with abundant surface AQP4 at a lesion edge (white arrow). (Scale bar, 33 μm.) (*E*) Myelin vacuolation in cerebellum of patient 2 (proteolipid protein immunoreactivity) (Scale bar, 50 μm.) (*F*) Same lesion as in *E* shows AQP4 partial internalization in an astrocyte (arrow) (Scale bar, 20 μm.)

injection. Detailed protocols for injection, membrane isolation, and hypotonic stress assays are provided in *SI Materials and Methods*.

Cell Lysate and Membrane Preparations. Cell lysates (NTE buffer: 100 mM NaCl; 10 mM Tris, pH 8.0; 1 mM EDTA; 0.5% Triton X-100) were clarified by centrifugation (10 min at 20,000 × *g*, 4 °C). Membranes were prepared as previously described (28). Protocols detailing membrane preparations and Western blot analysis are given in *SI Materials and Methods*.

Statistical Analysis. Error bars represent SD of the mean of at least three experiments. Statistical significance was calculated using Student's *t* test (two-tailed).

1. Nielsen S, et al. (1997) Specialized membrane domains for water transport in glial cells: High-resolution immunogold cytochemistry of aquaporin-4 in rat brain. *J Neurosci* 17:171–180.
2. Lennon VA, Kryzer TJ, Pittock SJ, Verkman AS, Hinson SR (2005) IgG marker of optic-spinal multiple sclerosis binds to the aquaporin-4 water channel. *J Exp Med* 202:473–477.
3. Hinson SR, McKeon A, Lennon VA (2010) Neurological autoimmunity targeting aquaporin-4. *Neuroscience* 168:1009–1018.
4. Hinson SR, et al. (2007) Pathogenic potential of IgG binding to water channel extracellular domain in neuromyelitis optica. *Neurology* 69:2221–2231.
5. Hinson SR, et al. (2008) Aquaporin-4-binding autoantibodies in patients with neuromyelitis optica impair glutamate transport by down-regulating EAAT2. *J Exp Med* 205:2473–2481.
6. Vincent T, et al. (2008) Functional consequences of neuromyelitis optica-IgG astrocyte interactions on blood-brain barrier permeability and granulocyte recruitment. *J Immunol* 181:5730–5737.
7. Marignier R, et al. (2010) Oligodendrocytes are damaged by neuromyelitis optica immunoglobulin G via astrocyte injury. *Brain* 133:2578–2591.
8. Saadoun S, et al. (2010) Intra-cerebral injection of neuromyelitis optica immunoglobulin G and human complement produces neuromyelitis optica lesions in mice. *Brain* 133:349–361.
9. Wolburg H (1995) Orthogonal arrays of intramembranous particles: A review with special reference to astrocytes. *J Hirnforsch* 36:239–258.
10. Wolburg H, Wolburg-Buchholz K, Fallier-Becker P, Noell S, Mack AF (2011) Structure and functions of aquaporin-4-based orthogonal arrays of particles. *Int Rev Cell Mol Biol* 287:1–41.
11. Furman CS, et al. (2003) Aquaporin-4 square array assembly: Opposing actions of M1 and M23 isoforms. *Proc Natl Acad Sci USA* 100:13609–13614.
12. Roemer SF, et al. (2007) Pattern-specific loss of aquaporin-4 immunoreactivity distinguishes neuromyelitis optica from multiple sclerosis. *Brain* 130:1194–1205.
13. Popescu BF, et al. (2011) Neuromyelitis optica unique area postrema lesions: Nausea, vomiting, and pathogenic implications. *Neurology* 76:1229–1237.
14. McKeon A, et al. (2008) CNS aquaporin-4 autoimmunity in children. *Neurology* 71:93–100.
15. Van Hoek AN, et al. (2009) Vasopressin-induced differential stimulation of AQP4 splice variants regulates the in-membrane assembly of orthogonal arrays. *Am J Physiol Renal Physiol* 296:F1396–F1404.
16. Preston GM, Carroll TP, Guggino WB, Agre P (1992) Appearance of water channels in Xenopus oocytes expressing red cell CHIP28 protein. *Science* 256:385–387.
17. Wallace RA, Jared DW, Dumont JN, Sega MW (1973) Protein incorporation by isolated amphibian oocytes. 3. Optimum incubation conditions. *J Exp Zool* 184:321–333.
18. Barnum SR (1995) Complement biosynthesis in the central nervous system. *Crit Rev Oral Biol Med* 6:132–146.
19. Hinson SR, et al. (2009) Prediction of neuromyelitis optica attack severity by quantitation of complement-mediated injury to aquaporin-4-expressing cells. *Arch Neurol* 66:1164–1167.
20. Crane JM, Tajima M, Verkman AS (2010) Live-cell imaging of aquaporin-4 diffusion and interactions in orthogonal arrays of particles. *Neuroscience* 168:892–902.
21. Pittock SJ, et al. (2006) Neuromyelitis optica brain lesions localized at sites of high aquaporin 4 expression. *Arch Neurol* 63:964–968.
22. Magaña SM, et al. (2009) Posterior reversible encephalopathy syndrome in neuromyelitis optica spectrum disorders. *Neurology* 72:712–717.
23. Conner SD, Schmid SL (2003) Regulated portals of entry into the cell. *Nature* 422:37–44.
24. Papanastasiou D, Poulas K, Kokla A, Tzartos SJ (2000) Prevention of passively transferred experimental autoimmune myasthenia gravis by Fab fragments of monoclonal antibodies directed against the main immunogenic region of the acetylcholine receptor. *J Neuroimmunol* 104:124–132.
25. McCarthy KD, de Vellis J (1978) Alpah-adrenergic receptor modulation of beta-adrenergic, adenosine and prostaglandin E1 increased adenosine 3′:5′-cyclic monophosphate levels in primary cultures of glia. *J Cyclic Nucleotide Res* 4:15–26.
26. Lennon VA, Ermilov LG, Szurszewski JH, Vernino S (2003) Immunization with neuronal nicotinic acetylcholine receptor induces neurological autoimmune disease. *J Clin Invest* 111:907–913.
27. Romero MF, Fong P, Berger UV, Hediger MA, Boron WF (1998) Cloning and functional expression of rNBC, an electrogenic Na(+)-HCO3- cotransporter from rat kidney. *Am J Physiol* 274:F425–F432.
28. Neely JD, Christensen BM, Nielsen S, Agre P (1999) Heterotetrameric composition of aquaporin-4 water channels. *Biochemistry* 38:11156–11163.

www.manaraa.com